

Journal of Materials Chemistry A

Accepted Manuscript



This is an *Accepted Manuscript*, which has been through the Royal Society of Chemistry peer review process and has been accepted for publication.

Accepted Manuscripts are published online shortly after acceptance, before technical editing, formatting and proof reading. Using this free service, authors can make their results available to the community, in citable form, before we publish the edited article. We will replace this *Accepted Manuscript* with the edited and formatted *Advance Article* as soon as it is available.

You can find more information about *Accepted Manuscripts* in the [Information for Authors](#).

Please note that technical editing may introduce minor changes to the text and/or graphics, which may alter content. The journal's standard [Terms & Conditions](#) and the [Ethical guidelines](#) still apply. In no event shall the Royal Society of Chemistry be held responsible for any errors or omissions in this *Accepted Manuscript* or any consequences arising from the use of any information it contains.



Journal Name

ARTICLE

A microcontact impedance study on NASICON-type $\text{Li}_{1+x}\text{Al}_x\text{Ti}_{2-x}(\text{PO}_4)_3$ ($0 < x < 0.5$) single crystals

Received 00th January 20xx,
Accepted 00th January 20xx

DOI: 10.1039/x0xx00000x

www.rsc.org/

D. Rettenwander^{a*}, A. Welzl^b, S. Pristat^c, F. Tietz^{c,d}, S. Taibl^b, G. J. Redhammer^a, J. Fleig^b

We successfully demonstrated the applicability of microcontact impedance spectroscopy (MC IS) on Li^+ conducting solid electrolytes and measured the Li^+ bulk conductivity (σ_b) of $\text{LiTi}_2(\text{PO}_4)_3$ (LTP) and $\text{Li}_{1+x}\text{Al}_x\text{Ti}_{2-x}(\text{PO}_4)_3$ (LATP) single crystals independent of microstructural effects (*e.g.*, grain boundaries, pores, density). The crystals had a size of about 100 μm in each direction and crystallized with NASICON-type structure ($R\bar{3}c$). Finite element calculations were performed to validate the impedance data analysis. A strong increase in σ_b in the order of three magnitudes (3.16×10^{-6} to $1.73 \times 10^{-3} \text{ S cm}^{-1}$) was found after incorporating 0.1 mol Al^{3+} per formula unit into LTP. Moreover, since the crystal structural changes are almost linear in the LATP system up to $x = 0.5$, the increase of σ_b is most probably related to additional Li^+ sites at the M_3 (36f) position. The additional Li^+ leads to a displacement of Li^+ occupying the M_1 (6b) sites towards the nearest-neighboring M_3 position, and therefore opens the fast-conducting pathway within the NASICON structure. A significant change in σ_b was also observed as the Al^{3+} content further increased ($x = 0.1$ to 0.5). The highest σ_b value of $5.63 \times 10^{-3} \text{ S cm}^{-1}$ was obtained for samples with $x = 0.4$.

1. Introduction

$\text{Li}_{1+x}\text{Al}_x\text{Ti}_{2-x}(\text{PO}_4)_3$ (LATP) with a NASICON-type structure (**Na Super-Ionic Conductor** with space group $R\bar{3}c$) is a solid electrolyte with Li^+ ion conductivity of approximately $10^{-4} - 10^{-3} \text{ S cm}^{-1}$, which makes it acceptable for the construction of an all-solid state Li-ion battery.¹⁻⁵ NASICON was originally discovered in 1976 by Hong et al. as an isostructural Na^+ -conducting material, namely $\text{Na}_{1+x}\text{Zr}_2\text{P}_{3-x}\text{Si}_x\text{O}_{12}$.^{6,7} Thereafter, Na^+ was replaced by Li^+ to obtain the Li^+ conducting counterpart. However, replacing Na^+ with Li^+ in $\text{LiZr}_2(\text{PO}_4)_3$ led to disappointingly low total Li^+ conductivity (σ_{total}) of only $\sim 10^{-9} \text{ S cm}^{-1}$ at room temperature (RT). A great enhancement of the Li^+ conductivity up to $10^{-6} \text{ S cm}^{-1}$ at RT can be achieved by substituting Zr^{4+} with the smaller Ti^{4+} .⁸ The additional partial substitution of Ti^{4+} by trivalent cations (*e.g.*, Al^{3+}) made LATP one of the best Li^+ -conducting materials among all inorganic Li^+ solid electrolytes.^{9,10} Apart from the chemical composition and crystal chemistry, it was also shown that sintering aids or binders (*e.g.*, $\text{Li}_4\text{P}_2\text{O}_7$, and Li_2O) led to an additional enhancement of the overall Li^+ conductivity in NASICON-based materials, regardless of the type and size of

the trivalent cation used.¹¹

The Li^+ conductivity of solid electrolytes is usually measured by impedance spectroscopy, which allows the separation of grain and grain boundary contributions. However, due to the very high Li^+ bulk conductivity (σ_b) of LATP ($> 10^{-3} \text{ S cm}^{-1}$), the corresponding arc in the complex impedance plane is in the high MHz range and can be conventionally resolved only at very low temperatures.^{12,13}

Determination of the bulk conductivity is strongly simplified when large sized single crystals are available; as for polycrystalline pellets macroscopic electrodes may be used in electrical measurements and electrical properties can be determined without being restricted by the need for a proper separation of partly large grain boundary resistances. For LATP, however, as for many other oxides, such large single crystals are not available. Here, a modification of conventional impedance spectroscopy comes into play: microelectrodes deposited on large grains of a polycrystalline sample still allow impedance measurements which are unaffected by the resistivity of grain boundaries.¹⁴⁻¹⁶ This is caused by the spatially very constricted current distribution between neighboring microelectrodes. However, so far this technique of local impedance measurements was rarely applied to determine bulk conductivities in small single crystals. Rather, properties of individual grain boundaries in polycrystalline materials were determined^{15,17,18} or local bulk conductivities were analyzed in extended samples with conductivity gradients.¹⁹

In this contribution, for the first time micro-contact impedance spectroscopy (MC IS) was applied to small LTP and LATP single crystals to exactly determine the Li^+ bulk conductivity at room

^a Department of Chemistry and Physics of Materials, University of Salzburg, 5020 Salzburg, Austria.

^b Institute for Chemical Technologies and Analytics, Vienna University of Technology, 1060 Vienna, Austria.

^c Institute of Energy and Climate Research, Materials Synthesis and Processing (IEK-1), Forschungszentrum Jülich GmbH, 52425 Jülich, Germany.

^d Helmholtz-Institute Münster, c/o Forschungszentrum Jülich GmbH, 52425 Jülich, Germany.

temperature. The resulting Li^+ conductivity is thus independent of microstructural effects (e.g., grain sizes, grain boundaries, density/porosity). In addition, the single crystals were carefully characterized by single crystal X-ray diffraction (SCXRD) and this enables a precise analysis of the impact of Al^{3+} substitution (e.g., crystal structure, Li^+ content) on transport properties and a better understanding of the structure-property relationship of Li^+ -based NASICON materials.

2. Experimental

2.1. Description of samples

Synthesis. Polycrystalline samples of LAMP with $0 < x < 0.5$ were synthesized using conventional solid state reaction. The stoichiometric amounts of Li_2CO_3 (VWR International, Belgium, 99 %), TiO_2 (VWR International, Belgium, 99 %), Al_2O_3 (Alfa Aesar, 99.99 %) and $(\text{NH}_4)\text{H}_2\text{PO}_4$ (Merck, 99 %), plus an excess of 10 wt% Li were mixed and homogenized in a mortar. Before use, the TiO_2 was dried at 600 °C for 6 h; all other reagents were used directly as received. Then, pellets with a diameter of 13 mm were pressed with 190 MPa and slowly heated in a Pt crucible with 120 K/h up to 1000 °C for 6 h in air and cooled down to RT with 300 K/h. After this calcination step, the pellets were crushed, homogenized in a mortar and again pressed to pellets. During a second heat treatment, the pellets were sintered at 1000 °C for 720 h (1 month) in a corundum crucible. During this period the powder particles grew to grains of nearly cubic shape with crystal edges of up to 150 μm . Small single crystals were easily obtained after crushing the pellet and sieving the coarse powder with a mesh size of 64 μm .

Scanning electron microscopy (SEM) analysis was carried out using a ZEISS Ultra Plus device. LTP and LAMP single crystals were embedded in an epoxy resin and polished with diamond paste. For the analysis, special attention was paid to grain and microelectrode sizes using a back-scattered electron detector (BSE). Energy dispersive X-ray spectroscopy (EDS) measurements were undertaken to measure the atomic ratios of Ti, Al, and P.

Inductively coupled plasma optical emission spectroscopy (ICP-OES). A small part of the sieved crystals was used to control the stoichiometry using a Thermo Scientific iCAP7600 spectrometer.

Single-crystal X-ray diffraction and crystal chemistry. The crystal structures of LTP and LAMP single crystals were carefully studied by SCXRD. Intensity data were collected on a Bruker SMART APEX CCD diffractometer using graphite-monochromatized Mo K_α radiation (50 kV, 30 mA). For the whole substitutional series, the space group $R\bar{3}c$ was confirmed. Basic structural data are compiled in Table 1. More details on the crystal structural study of the samples used here can be found elsewhere in a forthcoming paper.

In order to understand the crystallographic termini used in this investigation, a short description of the crystal structure of LTP and LAMP is provided in Figure 1.

The main results of the structural study are the following: The substitution of Al^{3+} exclusively takes place on the octahedral M_2 position, reducing the average $\text{M}_2\text{-O}$ bond lengths and also the polyhedral volume (Table 1). This – in sum – leads to a shrinkage of the unit cell parameters, predominantly along the c-axis (Table 1).

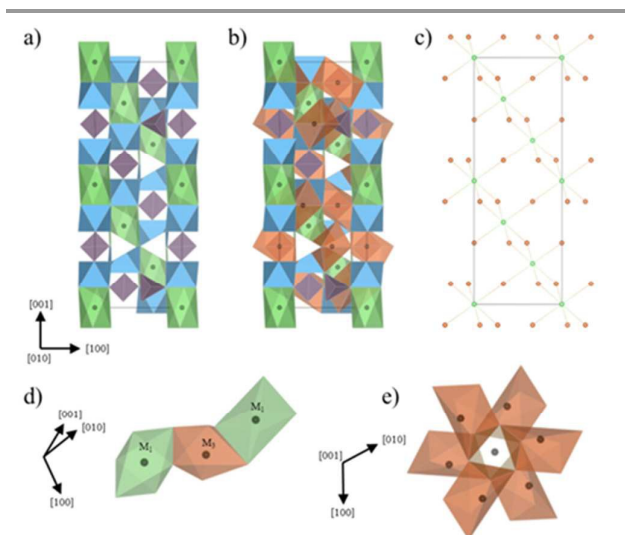


Figure 1. Crystal structure (Space group $R\bar{3}c$) of $\text{LiTi}_2(\text{PO}_4)_3$ (a) and $\text{Li}_{1-x}\text{Al}_x\text{Ti}_{2-x}(\text{PO}_4)_3$ (b). Green ($\text{M}_1/6b$) and orange ($\text{M}_2/36f$) octahedra are occupied by Li^+ . Blue octahedra ($\text{M}_2/12c$) are occupied by Ti^{4+} ($r^{\text{M}}(\text{Ti}^{4+}) = 0.605 \text{ \AA}^{14}$) or Al^{3+} ($r^{\text{M}}(\text{Al}^{3+}) = 0.530 \text{ \AA}^{20}$). The violet tetrahedra are occupied by P^{5+} (18e). O^{2-} are located at the corners of the polyhedra (not shown - Wyckoff position 36f). (c) Li^+ connectivity within the NASICON structure formed by M_1 and M_3 sites. (d) and (e) show the connections between M_1 and M_3 sites.

Table 1. Crystal chemical data of $\text{Li}_{1-x}\text{Al}_x\text{Ti}_{2-x}(\text{PO}_4)_3$ single crystals used in this study.^a

x =	0.0	0.1	0.2	0.3	0.4	0.5
SG	$R\bar{3}c$	$R\bar{3}c$	$R\bar{3}c$	$R\bar{3}c$	$R\bar{3}c$	$R\bar{3}c$
a	8.518	8.512	8.507	8.500	8.496	8.490
c	20.86	20.84	20.83	20.81	20.79	20.76
V	1311	1308	1305	1302	1299	1296
V_{M_1}	13.39	13.33	13.34	13.33	13.41	13.35
V_{M_2}	12.78	12.72	12.67	12.62	12.58	12.53
$U_{\text{iso}}^{\text{Li}_{\text{M}_1}}$ ^b	-	5.560	6.133	6.711	7.189	8.333

^aUnits of the quantities are \AA for a, c, \AA^3 for V, polyhedral V_{M_1} , and V_{M_2} . ^bThe equivalent isotropic displacement parameter ($U_{\text{iso}}^{\text{Li}_{\text{M}_1}}$) for Li^+ located at the M_1 site ($U_{\text{iso}}^{\text{Li}_{\text{M}_3}}$ can only be indicated, due to low intense residual electron density peaks at the M_3 site and is therefore not given here)

The M_1 position at (0, 0, 0) is occupied by Li. In due course of the proceeding substitution of Ti^{4+} by Al^{3+} , additional Li^+ is incorporated at the M_3 position at (0.07, 0.34, 0.09). The content of Li^+ scales very well with the amount of Al^{3+} . Hence, the Li^+ -conductivity path is along $\text{M}_1\text{-M}_3\text{-M}_1$ of the general NASICON structure type.

2.2. Preparation of microelectrodes on single crystals

The patterning of the microelectrodes was performed by photolithography. Therefore, a negative photoresist was coated on top of the embedded and polished single crystals (see Figure 2). After applying the mask with the appropriate microelectrode pattern – in our case, circular electrodes with a diameter of 30 μm – the samples were exposed to UV light. Areas which were covered during exposure were removed using a developer solution (Microresist Technologies, Germany). In a subsequent step, the microstructure was produced by ion beam etching.

2.3. Microcontact impedance spectroscopy

The electrochemical characterization of LTP and LATP was carried out by electrical impedance spectroscopy. All impedance measurements were performed at room temperature using an Alpha-A High Resolution Dielectric Analyzer with a ZG-2 interface (Novocontrol, Germany) in the frequency range between 3×10^6 Hz and 10^2 Hz with a voltage of 100 mV. Figure 3 shows the microcontact set-up and a schematic picture of the experiment performed.

For the evaluation of the impedance data, the complex nonlinear least-square fit software ZView (Scribner, USA)²¹ was used.

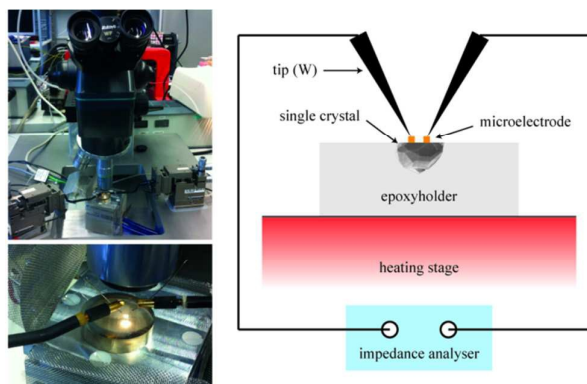


Figure 3. Sketch and photograph of the microcontact set-up.

2.4. Finite element calculation

Two circles with a diameter d of 30 μm were placed at different positions on top of various rectangular samples in order to investigate the relationship between measured resistance and geometrical parameters. The geometry is given in Table 2 and illustrated in Figure 4.

The voltage of the two microelectrodes was set to -0.5 V and 0.5 V, respectively. The Li^+ conductivity (σ) was chosen close to the experimentally obtained value of 5×10^{-3} S cm^{-1} (see below).

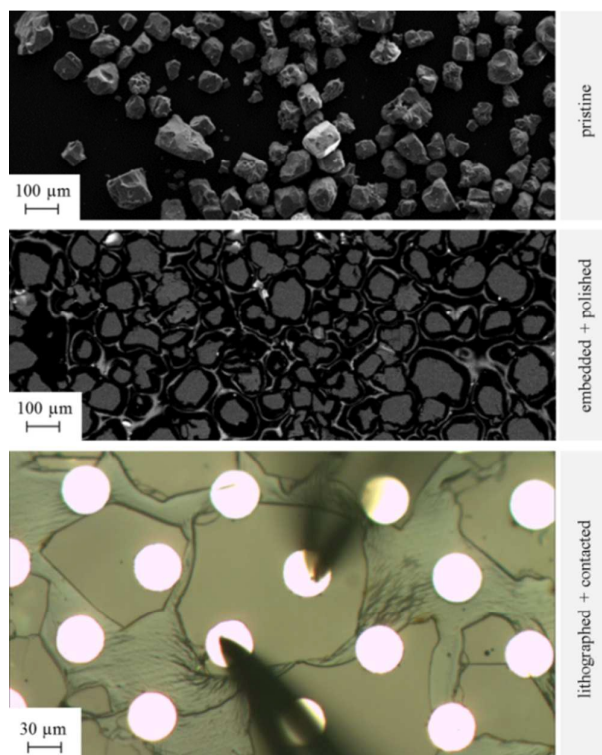


Figure 2. Top: Individual crystals after preparation, cleaning and sieving. Middle: Embedded and polished single crystals with patterned electrodes. White areas are lithographically prepared Ti/Pt microelectrodes, with a diameter of 30 μm . The black triangles are WC needles used to contact the electrodes.

Table 2. Geometrical factors for finite element calculations^a

case	a	b	c	r	s
1	.15	.15	.15	.045	.06
2	.15	.15	.15	.02	.06
3	.15	.15	.05	.045	.06
4	.10	.10	.10	.02	.06
5	.10	.05	.05	.02	.06
6	.30	.30	.30	.1	.1
7	.40	.40	.40	.133	.133
8	3	3	3	1	1
9	6	6	6	2	2
10	12	12	12	4	4

^a Values are given in mm. Circles represent microelectrodes with $\varnothing = 0.03$ mm.

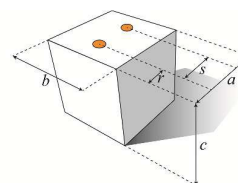


Figure 4. Sketch of the model used for finite element calculations. Circular microelectrodes are 30 μm in diameter.

The nodal voltages (Φ) were calculated using the Laplace equation

$$\nabla \cdot \sigma \nabla \Phi = 0 \quad (1)$$

and the current densities J were derived from Φ with Ohm's law

$$J = -\sigma \nabla \Phi. \quad (2)$$

The current was afterwards calculated by integrating the current density

$$I = \int_A j dA, \quad (3)$$

of the bc -plane placed at $a/2$. The resistance R was calculated based on

$$R = U/I. \quad (4)$$

Afterwards, the correction factor

$$f = R/R_{ideal}, \quad (5)$$

was determined to quantify deviations from the idealized analytic solution

$$R_{ideal} = 1/(\sigma d). \quad (6)$$

The latter was twice the ideal spreading resistance resulting from one circular microelectrode on a semi-infinite sample.²²

3. Results and discussion

3.1. Chemical composition and homogeneity

An SEM-BSE picture of the embedded crystals is shown in Figure 2. The single crystals were about 100 – 200 μm in size; the microelectrodes were about 28 μm in size. The qualitative composition of the single crystals obtained by SEM-EDS measurements (without Li) indicates almost perfect agreement between the measured and the intended chemical composition. The crystals within one compositional batch show no significant variation in stoichiometry. The single crystals have no pores, indicating a density of 100 %, therefore a possible impact of morphology and microstructure on the electrochemical properties can be excluded. The obtained analytical results using ICP-OES are listed in Table 3. In general, the analytical atomic ratios in Table 3 reflect very well the nominal composition.

Table 3: Analytical compositions of $\text{Li}_{1-x}\text{Al}_x\text{Ti}_{2-x}(\text{PO}_4)_3$ crystals investigated in this study.^a

x	Li	Al	Ti	P
0	1.013(17)	-	2.029(16)	2.958(25)
0.1	1.119(11)	0.110(1)	1.940(12)	2.931(12)
0.2	1.216(22)	0.212(4)	1.836(14)	2.936(25)
0.3	1.313(11)	0.321(2)	1.725(8)	2.942(12)
0.4	1.442(17)	0.418(2)	1.631(10)	2.910(12)
0.5	1.524(11)	0.504(2)	1.535(5)	2.936(25)

^a per formula unit (pfu).

There are, however, several small deviations which seem to indicate systematic differences to the starting compositions: 1) although the sum of atomic contents of Al, Ti and P gives always values between 4.96 and 4.99 reflecting very well the theoretical value of 5 cations per formula unit, the amount of P is always 2-3 % smaller than the nominal stoichiometric value. 2) On the contrary, the amounts of Al and Ti are systematically slightly larger than expected, indicating that there might occur a small partial substitution of P with Al and/or Ti and resulting in a systematic non-stoichiometry in the crystals. 3) The amount of Li is also always about 0.5-1 % larger than expected. Since the crystals were exposed to 1000 $^{\circ}\text{C}$ for one month, it can be concluded that the small

stoichiometric deviations seem to be the equilibrated compositions.

3.2. Impedance spectra of LTP and LTP single crystals

Impedance spectra were measured on the embedded polished single crystals of all compositions. Figures 5a and b display the relevant data measured at RT.

LTP shows a complete high frequency semicircle. In the impedance spectra of the LTP samples the minimum of $|Z_{im}|$ indicates the beginning of the high frequency semicircle. Common to all spectra is a strong increase of the imaginary part of the impedance towards low frequencies with an almost constant angle in the complex impedance plane.

This low frequency impedance can be attributed to the electrode response and described by a resistance in parallel to a constant phase element (CPE₂) with impedance

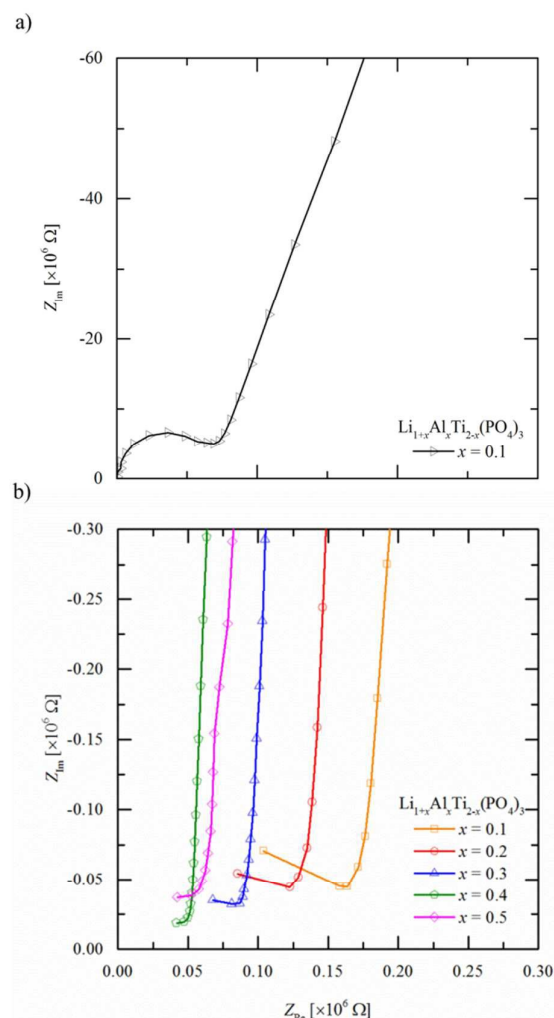


Figure 5. Impedance spectra of (a) LTP and (b) LTP samples with different Al content measured at room temperature. Data can be compared without normalization due to the same electrode geometry.

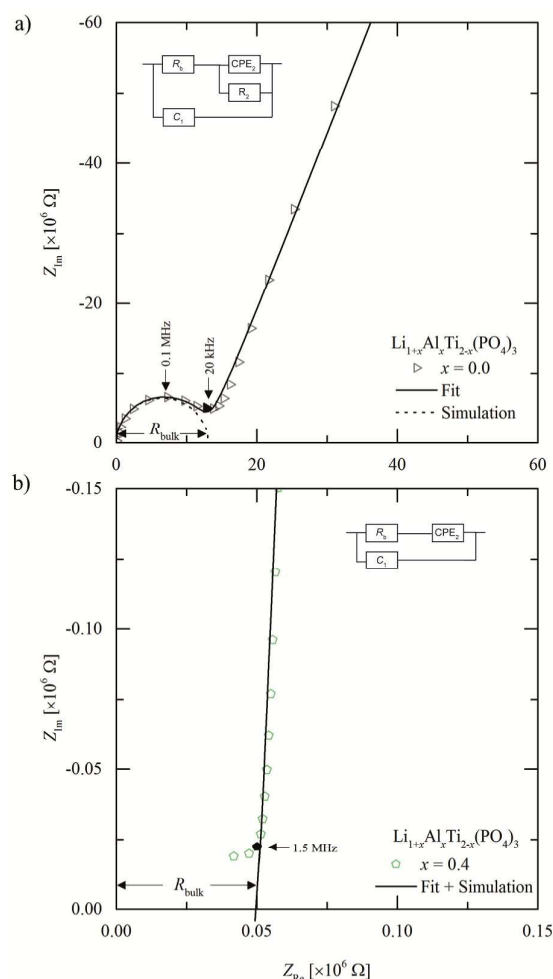


Figure 6. Equivalent circuit used to fit all spectra. Markers indicate frequencies of experimental data. In some cases R_2 was not required.

$$Z_{CPE} = 1/(i\omega)^n Q, \quad (7)$$

where ω is the phase frequency and the exponent n is a fit parameter reflecting the nonideal behavior of the capacitance. This electrode equivalent circuit is needed to analyze the sample-specific high-frequency arc of LTP samples, but does not provide any mechanistic information. The high-frequency arc represents the resistivity of the individual single crystals. The resistive part of the arc is simply fitted by a resistance element (R_b) and can be attributed to the volumetric Li^+ conduction (σ_b). The bulk capacitance (C_b) of LTP and LTP samples cannot be obtained, due to the unavoidable stray capacitance (C_1) ($C_1 \gg C_b$) introduced by the measurement set-up; here, C_1 is in the 100 fF range. The equivalent circuit used to fit the impedance spectra of LTP and LTP is shown in the inset of Figure 6 displaying representative fit examples of LTP and LTP with $x = 0.4$.

The spreading resistance of a circular microelectrode with an electrode diameter d of conductivity on half-infinite (*i.e.*, large) samples can be calculated by

$$R = (2d \sigma_b)^{-1}.^{22} \quad (8)$$

Table 4. Volumetric Li^+ bulk conductivities, σ_b , of $\text{Li}_{1-x}\text{Al}_x\text{Ti}_{2-x}(\text{PO}_4)_3$, with $0 < x < 0.5$ at RT obtained by microelectrodes.

x	R_b [Ω]	σ_b [S cm^{-1}]	RSD ^a [%]
0.0	$3.55 \times 10^{+5}$	3.13×10^{-6}	36
0.1	$6.41 \times 10^{+2}$	1.73×10^{-3}	11
0.2	$3.52 \times 10^{+2}$	3.16×10^{-3}	12
0.3	$2.16 \times 10^{+2}$	5.14×10^{-3}	10
0.4	$1.97 \times 10^{+2}$	5.63×10^{-3}	12
0.5	$2.36 \times 10^{+2}$	4.70×10^{-3}	17

^a Relative standard deviation of σ_b of 20 different single crystals per composition

For two microelectrodes in some distance, the approximation $R = (d \sigma_b)^{-1}$ (9) results and this was used to calculate σ_b from the R values given in Table 4.

3.3. Evaluation of the accuracy of MC IS measurements

Since Eq. 9 is an approximation, finite element calculations were employed to test its accuracy for measurements on small single crystals. On the one hand, the limited distance between the microelectrodes lowers the resistance compared to the idealized formula. On the other hand, the limited size of the single crystal enhances the resistance. This was quantified for different sample sizes and positions of microelectrodes (see Figure 4 and Table 2).

Current I and resistance R obtained by calculating the current density of the geometries used (*e.g.*, case 1 as illustrated in Figure 7) are given in Table 3. The corresponding correction factors f are also summarized in Table 5 and illustrated in Figure 8.

The current calculated for the (close-to-reality) geometries of cases 1–3 was in the range of 1.59 – 1.67×10^{-9} A, whereby the current decreased with a decreasing depth (c) of the box or when the microelectrodes move towards one edge. The correction factors f were in the range of 0.90 to 0.92, which represents an error of <10 % in determining R from Eq. 9.

In case 4, a cubic box that was one-third smaller than case 1 was chosen. Interestingly $f = 1$, which means there was no error in accuracy due to the compensation of distance and the size of the box (see above).

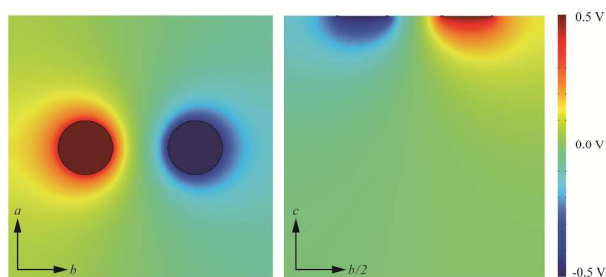
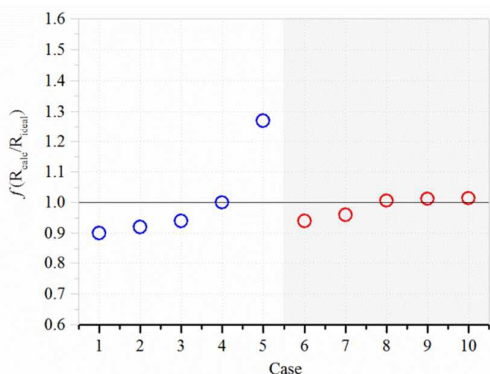


Figure 7. Potential distribution of case 1 calculated by the finite element method.

Table 5. Calculated current (I), resistivity (R), and correction factor (f)

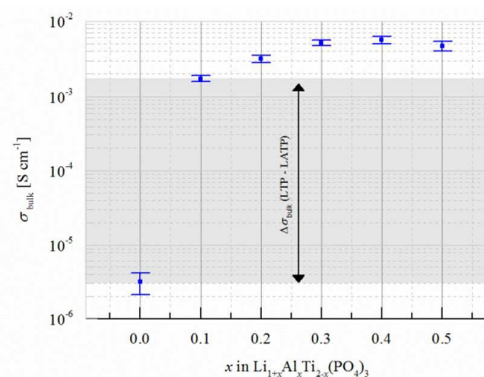
case	I [$\times 10^{-9}$ A]	R [$\times 10^{+8}$ Ω]	f
1	1.67	5.97	0.90
2	1.63	6.13	0.92
3	1.59	6.30	0.94
4	1.50	6.65	1.00
5	1.18	8.48	1.27
6	1.59	6.27	0.94
7	1.73	6.40	0.96
8	1.49	6.72	1.01
9	1.48	6.75	1.01
10	1.48	6.76	1.01

Figure 8. Calculated correction factors f of cases 1-10.

When the geometry was chosen to be very nonideal (case 5), an error of 27 % was obtained. Factor f should also approach 1 in the case of a very large box with microelectrodes at large distances from each other. As shown for cases 6–10, the f values converged to a value of $f = 1.01$, which indicates that the numerical calculations are reliable. Overall, this shows that Eq. 9 is appropriate to calculate Li^+ bulk conductivities from MC-IS measurements on small single crystals. Deviations due to differently sized single crystals or different microelectrode positions are generally in the 10 % range.

3.4. The Li^+ conductivity of LTP and LTP single crystals.

The σ_b values of LTP and LTP single crystals are shown in Figure 9 and given in Table 4.

Figure 9. Li^+ bulk conductivity (σ_b) of LTP as a function of Al^{3+} content. Error bars indicate the deviation of 20 measurements on different single crystals within one composition.

3.4.1. Electrochemical homogeneity.

The σ_b value of LTP is $2.81 \times 10^{-6} \text{ S cm}^{-1}$, which is in agreement with values reported previously (*e.g.*, Ref. 11). The only exception is the value of $1.6 \times 10^{-3} \text{ S cm}^{-1}$ as reported by Arbi et al. (note: this value is similar to values obtained for LTP).¹⁰

The relative standard deviation of σ_b values obtained from 20 different single crystals is 36 %, which is about three times larger than values obtained from LTP samples (see Table 4). This is most probably related to slight compositional inhomogeneities, which remain undetected by conventional characterization methods (*e.g.*, SEM-EDS), as proposed by Wang et al.¹² They observed two partly overlapping bulk arcs in the complex impedance plane of LTP samples, which they attributed to two electrically different regions within grains or single crystals caused by chemical inhomogeneities, such as core and shell (see below), even though the sample appeared to be structurally phase-pure and consisted of well-grown grains. They evaluated two different σ_b contributions from the different electrical regions and the values obtained from the reported Arrhenius plot are comparable to values measured here.¹²

The two arcs seen in the former study cannot be distinguished in our case due to the unavoidable stray capacitance, which makes the bulk capacitance inaccessible for analysis and also prevents a separation of two overlapping semicircles. Hence, it remains unknown whether inhomogeneities exist, even within one grain, or whether variations are present.

Arbi et al. made analogous observations for LTP samples.²³ They explained this phenomenon with the existence of a Li-poor shell structure and an Al-rich core for samples with low Al^{3+} content. The increase in Al^{3+} in LTP leads to a homogeneous grain composition and therefore to a single electrical bulk response.²³ Since in our samples containing 0.1–0.5 Al^{3+} per formula unit (pfu), no significant Li^+ conductivity variation was observed, we conclude chemical homogeneity within the LTP single crystals studied in this work. The incorporation of 0.1 Al^{3+} pfu. leads to an increase in σ_b of three orders of magnitude ($\sigma_b = 1.73 \times 10^{-3} \text{ S cm}^{-1}$), which is in agreement with results for samples of the same composition reported previously.¹⁰

3.4.2. The origin of the enhanced σ_b

In order to understand the origin of the high Li^+ bulk conductivity observed for LTP samples, Wang et al. performed a detailed impedance spectroscopy study in a wide temperature range (60 °C to -150 °C). For low temperatures, they were able to reveal the high-frequency arc in the complex impedance plane, *i.e.*, the feature due to Li^+ bulk conductivity and bulk permittivity.¹² Based on a previous study by Aono et al., who found a significant decrease in bulk and grain boundary resistance as a function of density in LTP/LATP ceramics^{9,11}, they concluded that there is a correlation between the low conductivity of LTP and the low density of those materials.

In contrast, Lang et al. recently published a detailed investigation on the role of the local structure of substitution variants of LTP on Li^+ mobility by means of density functional theory (DFT).²⁴ They showed that additional Li^+ is introduced by substituting Ti^{4+} by Al^{3+} and located in an energetically favored site (M_3). This occupation induces the nearest-neighbor M_1 site to displace towards the next M_3 site, which promotes an interstitial migration mechanism, in agreement with observations made by NMR spectroscopy.¹⁰ This diffusion mechanism is limited as a 1D pathway with $E_a = 0.19$ eV. An activation energy E_a of 0.20 eV is necessary to rearrange Li^+ in corresponding sites to open 3D diffusion in the Li^+ sublattice. Both E_a values are significantly lower compared to the activation energy in LTP ($E_a = 0.46(5)$)¹⁰.

Although the LTP and LTP samples in this study have identical relative densities and the crystal structural relationships by introducing Al^{3+} into the LTP structure are almost linear, nevertheless σ_b shows an increase of three orders of magnitude. Therefore, density and crystal structure can be excluded as reasons for enhanced Li^+ conduction.

The logical conclusion is that the increase in σ_b is based only on the incorporation of the additional Li^+ ions as highly mobile charge carriers opening the fast-diffusion pathways in the LTP-NASICON structure, as discussed by Lang et al. (see above).²⁴

3.4.3. σ_b of LTP as a function of the Al^{3+} content

The influence of the amount of Al^{3+} in LTP on σ_b is still a matter of discussion. As an example, Arbi et al. performed ^7Li NMR and EIS studies and found an increase in σ_b with an increasing amount of Al^{3+} (up to $x = 0.2$).¹⁰ Above $x = 0.2$, the grain interior conductivity remained almost constant, which was connected with an upper incorporation limit of Al^{3+} in LTP for their synthesis route. In contrast, Forsyth et al. and Takeda et al. showed by ^7Li NMR that the increase in the amount of Al^{3+} only introduced minor changes in the line widths, which indicates a minor influence of Al^{3+} on the Li^+ motion within the grain.^{25,26} In addition, Wang et al. (see above) interpreted their impedance spectroscopy study in such a way that Al^{3+} did not significantly affect σ_b in LTP samples, whereby the maximum σ_b ($7.7 \times 10^{-3} \text{ S cm}^{-1}$) was observed for samples with $x = 0.4$.¹²

The Li^+ conductivity in our study is the true Li^+ bulk conductivity and is not affected by the microstructure of a polycrystal. We clearly observed a significant increase as a

function of the Al^{3+} content up to $x = 0.4$ (up to $5.63 (\pm 0.68) \times 10^{-3} \text{ S cm}^{-1}$), which is in contrast to the aforementioned studies. For LTP crystals with $x = 0.5$, σ_b decreases slightly to $4.70 (\pm 0.80) \times 10^{-3} \text{ S cm}^{-1}$. Very recently, the bulk conductivity of LTP with $x = 0.5$ was separated from grain boundary contributions by impedance spectroscopy down to 123 K. Extrapolating the low-temperature data to RT, a value of $3.4 \times 10^{-3} \text{ S cm}^{-1}$ was derived, which is in very good agreement with our measurements.¹³

This increase in σ_b can be most probably attributed to increasing amounts of Li^+ occupying the M_3 sites and displacing the Li^+ in M_1 sites towards the nearest-neighbor M_3 sites. Therefore, the additional Li content further promotes the Li^+ diffusion, as discussed by Lang et al.²³ and Arbi et al.¹⁰, and further supported by the equivalent isotropic displacement parameter of our SCXRD study (see above). The resulting slight decrease in σ_b above $x = 0.4$ can be related to the intrinsic process described by Lang et al.²⁴ The Li^+ , which is needed for charge balancing the substitution of Ti^{4+} by Al^{3+} , favorably occupies the M_3 site next to a substituted Al^{3+} . This leads to a successive trapping of Li^+ as a function of the Al^{3+} content, which possibly becomes predominant with a critical amount of Al^{3+} in the lattice and slightly reduces the mobility of displaced Li^+ ions, which originally promoted the diffusion behavior in the LTP-LATP system.

Conclusions

The applicability of microcontact impedance spectroscopy to determine volumetric Li^+ bulk conductivities of $\text{LiTi}_2(\text{PO}_4)_3$ and $\text{Li}_{1+x}\text{Al}_x\text{Ti}_{2-x}(\text{PO}_4)_3$ single crystals at room temperature was successfully demonstrated. We were able to show that density can be excluded as a reason for the strong increase in σ_b of three orders of magnitude (3.12×10^{-6} to $1.73 \times 10^{-3} \text{ S cm}^{-1}$) after substitution with 0.1 mol Al^{3+} pfu in the LTP structure, which is in contrast to one of the prevailing considerations in previous studies. Moreover, since changes in the crystal structure are almost linear in the LTP-LATP system between $x = 0$ and $x = 0.5$, the strong increase in σ_b is related to the additional Li^+ at the M_3 position, which displaces the Li^+ at M_1 sites towards the next M_3 position resulting in fast-conducting ions within the NASICON structure. Finally, σ_b significantly increases as a function of the Al^{3+} content up to $5.63 \times 10^{-3} \text{ S cm}^{-1}$ for LTP samples with $x = 0.1$ – 0.4 .

Acknowledgements

This research was supported by the Austrian Science Fund (FWF): project number P25702. In addition, financial support from the Helmholtz Association with the framework of the project programs "Helmholtz Energy Alliance - stationary electrochemical solid-state storage and conversion" and "HGF initiative for mobile/stationary energy storage systems" is gratefully acknowledged. The authors thank Ms. M. T. Gerhards (IEK-1) for technical assistance during sample

preparation and colleagues from ZEA-3 of Forschungszentrum Jülich for the ICP-OES measurements.

Notes and references

- 1 L. Shi-Chun, L. Zu-Xiang, *Solid State Ionics*, 1983, **10**, 835.
- 2 S. Hamdoune, D. Tran Qui, E. J. L. Schouler, *Solid State Ionics*, 1986, **19**, 587-591.
- 3 H. Aono, E. Sugimoto, Y. Sadaoka, N. Imanaka, G.-Y. Adachi, *J. Electrochem. Soc.*, 1993, **140**, 1827.
- 4 A. D. Robertson, A. R. West, A. G. Ritchie, *Solid State Ionics*, 1997, **104**, 1.
- 5 J. M. Tarascon, M. Armand, *Nature*, 2001, **414**, 359.
- 6 H. Y.-P. Hong, *Mater. Res. Bull.*, 1976, **11**, 203.
- 7 J. B. Goodenough, H. Y.-P. Hong, J. A. Kafalas, *Mater. Res. Bull.*, 1976, **11**, 173.
- 8 J.-M. Winand, A. Rulmont, P. Tarte, *J. Solid State Chem.*, 1991, **93**, 341.
- 9 H. Aono, E. Sugimoto, Y. Sadaoka, N. Imanaka, G. Adachi, *J. Electrochem. Soc.*, 1990, **137**, 1023.
- 10 K. Arbi, S. Mandal, J. M. Rojo, J. Sanz, *Chem. Mater.*, 2002, **14**, 1091.
- 11 H. Aono, E. Sugimoto, Y. Sadaoka, N. Imanaka, G.-Y. Adachi, G., *Solid State Ionics*, 1991, **47**, 257.
- 12 S. Wang, L. Ben, H. Li, L. Chen, *Solid State Ionics*, 2014, **268**, 110.
- 13 S. Breuer, V. Epp, Q. Ma, F. Tietz, M. Wilkening, *J. Mater. Chem. A*, 2015, to be published.
- 14 J. Fleig, S. Rodewald, J. Maier, *J. Appl. Phys.*, 2000, **87**, 2372.
- 15 S. Rodewald, J. Fleig, J. Maier, *J. Am. Ceram. Soc.*, 2001, **84**, 521.
- 16 J. Fleig, S. Rodewald, J. Maier, *Solid State Ionics*, 2000, **136-137**, 905.
- 17 J. Fleig, J. Maier, *Phys. Chem. Chem. Phys.*, 1999, **1**, 3315.
- 18 J.-S. Lee, J. Fleig, J. Maier, D.-Y. Kim, *J. Mat. Res.*, 2004, **19**, 864.
- 19 J. Fleig, S. Rodewald, J. Maier, *J. Am. Ceram. Soc.*, 2000, **83**, 1969.
- 20 R. D. Shannon, C. T. Prewitt, C. T. *Acta Cryst.*, 1969, **B25**, 925.
- 21 D. Johnson, "Zview Version 3.2c", Scribner Associates Inc., 1990-2007.
- 22 J. Newman, *J. Electrochem. Soc.*, 1966, **133**, 501.
- 23 K. Arbi, M. Hoelzel, A. Kuhn, F. Garcia-Alvarado, J. Sanz, *Inorg. Chem.*, 2013, **52**, 9290-9296.
- 24 B. Lang, B. M. Ziebarth, C. Elsässer, *Chem. Mater.*, 2015, **27**, 5040.
- 25 M. Forsyth, S. Wong, K. M. Nairn, A. S. Best, P. J. Newman, D. R. MacFarlane, *Solid State Ionics*, 1999, **124** 213.
- 26 K. Takada, M. Tansho, I. Yanase, T. Inada, A. Kajiyama, M. Kouguchi, S. Kondo, M. Watanabe, *Solid State Ionics*, 2001, **139**, 241.
- 27 K. Arbi, W. Bucheli, R. Jimenez, J. Sanz, *J. Eur. Ceram Soc.*, 2015, **33**, 1477.

